

1 **F₁ region ion composition in Svalbard during the**
2 **International Polar Year 2007-2008**

3 **Ilkka I. Virtanen¹, Habtamu W. Tesfaw¹, Anita T. Aikio¹, Roger Varney²,**
4 **Antti Kero³, and Neethal Thomas³**

5 ¹Space Physics and Astronomy research unit, University of Oulu, Finland

6 ²Atmospheric and Oceanic Sciences, University of California Los Angeles, Los Angeles, California, USA

7 ³Sodankylä Geophysical Observatory, University of Oulu, Sodankylä, Finland

8 **Key Points:**

- 9
- 10 • We use novel data analysis techniques and chemistry modeling to fit atomic oxy-
 - 11 gen ion fractions to EISCAT Svalbard radar data during IPY.
 - 12 • We characterize the F₁ region ion composition dependence on local time, solar zenith
 - 13 angle, and geomagnetic activity.
 - 14 • The molecular-to-atomic ion transition altitudes are 14–32 km lower than those
 - predicted by the International Reference Ionosphere.

Corresponding author: Ilkka Virtanen, ilkka.i.virtanen@oulu.fi

Abstract

Ions in the F region ionosphere at 150–400 km altitude consist mainly of molecular NO^+ and O_2^+ , and atomic O^+ . Incoherent scatter (IS) radars are sensitive to the molecular-to-atomic ion density ratio, but its effect to the observed incoherent scatter spectra is almost identical with that of the ion temperature. It is thus very difficult to fit both the ion temperature and the fraction of O^+ ions to the observed spectra. In this paper, we introduce a novel combination of Bayesian filtering, smoothness priors, and chemistry modeling to solve for F_1 region O^+ ion fraction from EISCAT Svalbard IS radar (75.43° corrected geomagnetic latitude) data during the international polar year (IPY) 2007–2008. We find that the fraction of O^+ ions in the F_1 region ionosphere is controlled by ion temperature and electron production. The median value of the molecular-to-atomic ion transition altitude during IPY varies from 187 km at 16–17 MLT to 208 km at 04–05 MLT. The ion temperature has maxima at 05–06 MLT and 15–16 MLT, but the transition altitude does not follow the ion temperature, because photoionization lowers the transition altitude. A daytime transition altitude maximum is observed in winter, when lack of photoionization leads to very low daytime electron densities. Both ion temperature and the molecular-to-atomic ion transition altitude correlate with the Polar Cap North geomagnetic index. The annual medians of the fitted transition altitudes are 14–32 km lower than those predicted by the International Reference Ionosphere.

Plain Language Summary

Ions in the F region ionosphere at 150–400 km altitudes consist mainly of molecular NO^+ and O_2^+ , and atomic O^+ . Incoherent scatter radars are sensitive to the molecular-to-atomic ion density ratio, but its effect to the observed incoherent scatter spectra is almost identical with that of the ion temperature. It is thus very difficult to fit both the ion temperature and the fraction of O^+ ions to the observed spectra. This causes bias to the fitted temperatures and leaves behaviour of the F_1 region ion composition poorly known. We apply a novel combination of inverse mathematics and chemistry modeling to analysis of EISCAT Svalbard incoherent scatter radar data, and solve for both the ion temperature and the fraction of O^+ ions at the same time. We find that the ion composition is considerably different from a standard model, that it undergoes regular diurnal variations, and it is affected by geomagnetic activity. The typical variations can be qualitatively explained by known diurnal variations in ion temperature, solar photoionization, and ion chemistry. When the ionosphere above Svalbard is in almost complete darkness in mid-winter, ion composition in the daytime ionosphere is considerably different from that observed during the other seasons.

1 Introduction

Typical ion composition in the F region ionosphere makes a smooth transition from molecular NO^+ and O_2^+ below 150 km altitude to almost pure atomic O^+ around 350 km altitude. The ion composition is a key parameter that affects energy exchange rates between the ions and the thermospheric neutral particles, ion and neutral chemistry, and electron recombination speeds. The F region ion composition is a key unknown also in attempts to understand molecular ion upflow and outflow from the ionosphere to the magnetosphere (Takada et al., 2021). However, many aspects of the molecular-to-atomic ion transition remain unknown, because it occurs at too low altitudes for in situ satellite observations, and the ground-based incoherent scatter radar (ISR) observations cannot provide information about the ion composition without limiting assumptions about the ion or electron temperature if conventional analysis tools are used (Evans, 1967; Kelly & Wickwar, 1981). The so-called temperature ion composition ambiguity (TICA) (Martínez-Ledesma & Díaz Quezada, 2019) arises from the fact that changes in ion composition and ion temperature can lead to almost identical changes in the incoherent scatter spectra. As a con-

65 sequence, the ISR data do not only lack the ion composition information, but the ion
66 composition is typically taken from a model, and the ion and electron temperatures fit-
67 ted to the observed spectra are biased whenever the true ion composition is different from
68 the model values (Blelly et al., 2010).

69 Several different approaches have been proposed for solving the TICA problem. Lathuillere
70 et al. (1983) and Lathuillere and Pibaret (1992) used coarse resolutions in time and alti-
71 tude to reach such a high statistical accuracy in the observed incoherent scatter spec-
72 tra that both ion temperature and composition could be fitted without any extra infor-
73 mation. Kelly and Wickwar (1981) constrained the electron temperature in presence of
74 ion frictional heating and the ion temperature in presence of electron precipitation to
75 enable the ion composition fits. Bjørnå and Kirkwood (1988), Fredriksen (1990), and Aponte
76 et al. (2007) used the incoherent scatter plasma lines to gain the necessary extra infor-
77 mation about the electron density and electron temperature to enable the composition
78 fits, and Häggström and Collis (1990) used tri-static electric field measurements and ion
79 energy equation to reach the same goal. The most popular approach to overcome the
80 TICA problem has been the full-profile analysis, in which one assumes that the plasma
81 parameter altitude profiles are smooth, and the ion composition profile is often even as-
82 sumed to follow some pre-defined shape. These methods include both full-profile solvers
83 that actually fit the plasma parameters to the raw radar data (Cabrit & Kofman, 1997;
84 Litvine et al., 1998), and models to make corrections to the fitted plasma parameters (Shibata
85 et al., 2000; Blelly et al., 2010; Zettergren et al., 2010).

86 The techniques listed above have not made their way to routine EISCAT radar data
87 analysis for several reasons, for example because coarse altitude resolutions of tens of kilo-
88 meters and integration times of several minutes are typically not acceptable, the plasma
89 lines are not always detectable and their analysis is tedious, and the true full-profile solvers
90 require considerable computing power if one wants to include also the E region, which
91 requires high altitude resolution, in the same analysis. A computationally light-weight
92 solution that resembles the full-profile analysis, and even extends the principle to an as-
93 sumption of smoothness in time, was proposed by Virtanen et al. (2021). The Bayesian
94 Filtering Module (BAFIM) is able to fit F₁ region ion compositions in relatively quiet
95 conditions, but the authors concluded that support from a chemistry model would be
96 needed to better capture rapid ion temperature and composition variations in active con-
97 ditions. Chemistry modeling is already in use in AMISR radar data analysis (Richards
98 et al., 2009), in which the ion composition is modelled in each range gate separately by
99 a chemistry model called the Ion Density Calculator (IDC) (Richards et al., 2010; Richards,
100 2011). The same chemistry model is used also in the latest versions of the International
101 Reference Ionosphere (Bilitza et al., 2022).

102 In this paper we combine the BAFIM tool (Virtanen et al., 2021) with the IDC (Richards
103 et al., 2010; Richards, 2011) to carry out IS radar data analysis in a way that produces
104 reliable estimates of the fraction of O⁺ ions and ion temperature in the F region. The
105 chemistry model is coupled with BAFIM in such a way that it guides the solver towards
106 physically reasonable solutions, but does not force the final solution to exactly match
107 with the chemistry model. This approach allows us to use the model also when the neu-
108 tral background ionosphere is not exactly known or when the ions are not in chemical
109 equilibrium. We apply the technique to the almost continuous one-year EISCAT Sval-
110 bard incoherent scatter radar run conducted during the International Polar Year (IPY)
111 from March 2007 to February 2008, and study the statistical properties of ion compo-
112 sition, ion temperature, and electron density at 75.43° corrected geomagnetic latitude,
113 corresponding typically to the polar cap location. Statistical results of the F region ion
114 composition from high-latitude radars have been previously provided only by Litvine et
115 al. (1998), who used about 1200 h of data from the EISCAT Tromsø radar site in the
116 auroral oval, and by Shibata et al. (2000) who used 528 h of data from the same site.
117 To our knowledge, our study is the first to provide statistics of F₁ region ion composi-

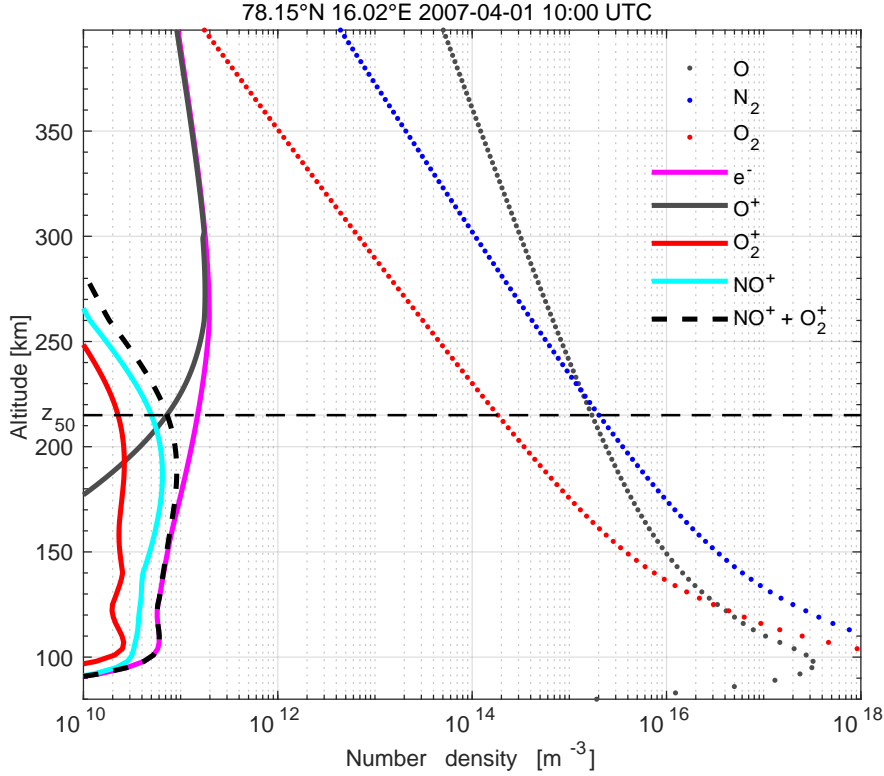


Figure 1. Neutral and charged particle density profiles in Svalbard on April 1 2007 at 10:00 UTC, calculated with the NRLMSISE-00 and IRI-2020 models, respectively. The horizontal dashed line shows the molecular-to-atomic ion transition altitude z_{50} .

118 tion from a polar cap ISR. Our about 5000 h data set is also larger than those in the pre-
 119 vious studies, although it was collected during only one year, during solar minimum con-
 120 ditions.

121 The paper is organized as follows. In Section 2 we shortly review the typical ion
 122 and neutral compositions in the E and F region ionosphere, as well as the basic ion chem-
 123 ical reactions and atmospheric dynamics that alter the ion composition. In Section 3 we
 124 introduce the data and the data analysis technique, and give an example of the analy-
 125 sis results. Statistical results from one year of data are presented in Section 4, the key
 126 findings are discussed in more detail in Section 5, and the final conclusions are given in
 127 Section 6.

128 2 F-region ion and neutral composition and chemistry

129 Examples of typical number densities of the major ion and neutral species in the
 130 E and F regions of the ionosphere are shown in Figure 1. The ion densities are calcu-
 131 lated with the International Reference Ionosphere (IRI) model version 2020 (Bilitza et
 132 al., 2022), and the neutral densities with the Naval Research Laboratory Mass Spectrom-
 133 eter and Incoherent Scatter radar (NRLMSISE-00) model (Picone et al., 2002). The model
 134 values are calculated for geographic coordinates of the EISCAT Svalbar radar (78.15°
 135 N, 16.02 ° E) for 01 April 2007 10:00 UTC. The figure shows that, in this case, the molec-
 136 ular NO^+ and O_2^+ form almost 100 % of the ion density in the E and lower F regions

137 up to 180 km altitude. A smooth transition from the molecular ions to atomic O^+ takes
 138 place between 180 and 270 km altitudes, and the ion gas is almost 100 % O^+ above 270 km.
 139 The molecular-to-atomic ion transition altitude z_{50} , where total number density of the
 140 molecular ions ($NO^+ + O_2^+$) is equal to the atomic O^+ ion density, is shown as a hor-
 141 izontal dashed line at 215 km altitude. The ion composition reflects altitude variations
 142 in the neutral composition, in which the molecular N_2 and the atomic O are the dom-
 143 inant species below and above 230 km altitude, respectively. The altitudes given above
 144 are only illustrative, because the densities undergo both diurnal and seasonal variations,
 145 and are affected by solar activity.

146 Ions are produced by solar EUV and soft X ray radiation, impact ionization by pre-
 147 cipitating particles, and in chemical reactions. They are lost via recombination and re-
 148 arrangement reactions. The molecular NO^+ and O_2^+ ions are lost mainly via dissocia-
 149 tive recombination in the reactions



150 where α_1 and α_2 are the reaction rates of the reactions (1) and (2), correspondingly. As
 151 recombination of atomic O^+ is very slow, the atomic O^+ ions are lost mainly via rear-
 152 rangement with neutral N_2 and O_2 in the reactions



153 where k_1 and k_2 are the corresponding reaction rates. The molecular NO^+ and O_2^+ ions
 154 produced in the rearrangement reactions (3) and (4) are subsequently lost via the dis-
 155 sociative recombination reactions (1) and (2). For details of the ion chemical reactions
 156 and their reaction rates, we refer to Richards (2011).

157 The ion composition may undergo rapid variations during ion frictional heating and
 158 particle precipitation events. The ion heating speeds up the loss of atomic O^+ and the
 159 production of molecular NO^+ in the rearrangement reaction (3) between O^+ and N_2 ,
 160 because the reaction rate k_1 is proportional to square of the ion temperature in high tem-
 161 peratures (Kelly & Wickwar, 1981; Richards, 2011). The heating may also drive ther-
 162 mal expansion of the neutral atmosphere, which increases the neutral N_2 and O_2 den-
 163 sities in the F region and thus speeds up the production of molecular NO^+ and O_2^+ in
 164 the rearrangement reactions (3) and (4). On the other hand, the molecular NO^+ and
 165 O_2^+ ions undergo dissociative recombination with the free electrons (reactions 1 and 2).
 166 The net effect is that ion frictional heating tends to increase the fraction of molecular
 167 ions out of the total ion content, but to decrease the total ion (electron) number den-
 168 sity. Electron production, either by photoionization or by particle precipitation, increases
 169 the total ion density and the fraction of the atomic O^+ ions, because the higher electron
 170 density speeds up the dissociative recombination reactions (1) and (2) but does not af-
 171 fect the rearrangement reactions (3) and (4) (Kelly & Wickwar, 1981). The above sug-
 172 gests that the neutral composition, the ion production rate and the ion temperature are
 173 the key factors that control the ion composition.

174 3 Data and data analysis

175 We use a novel combination of advanced inverse mathematics and chemistry mod-
 176 eling to solve for the electron density N_e , electron temperature T_e , ion temperature T_i ,
 177 line-of-sight bulk plasma velocity V_i , and the fraction of atomic O^+ ions out of the to-
 178 tal ion content p from one year of EISCAT Svalbard radar data, collected during the IPY
 179 2007–2008. This section describes the data and the analysis technique.

180

3.1 ESR IPY data

181

182

183

184

185

186

187

188

189

190

From March 2007 until February 2008 the EISCAT Scientific Association operated the EISCAT Svalbard radar (ESR) almost continuously in the same operation mode, as opposed to the usual campaign-based operations with a variety of observation modes. The so-called ipy-mode used the field-aligned 42 m antenna and produced samples of the incoherent scatter autocorrelation function with 6 s time resolution. The experiment covers altitudes from the D region up to 509 km altitude and uses alternating codes (Lehtinen & Häggström, 1987) with 30 μ s bit length. The data are sampled with 15 μ s sampling steps, which leads to 4.5 km range resolution at "full" (multiples of 30 μ s) ACF lags and to 2.25 km resolution at the fractional (15, 45, 75, ... μ s) lags (Huuskonen et al., 1996). We call these data "the IPY data".

191

192

193

194

195

196

197

EISCAT has conducted plasma parameter fits to the IPY data using the Grand Unified Incoherent Scatter Design and Analysis Package (GUISDAP) (Lehtinen & Huuskonen, 1996) and these data are available in the Madrigal data base. The fitted parameters are N_e, T_e, T_i , and V_i . The fraction of O^+ ions p is taken from the IRI model in the standard GUISDAP analysis. It is well known that the IRI ion compositions are inaccurate in the F₁ region, which leads to artefacts in ion and electron temperatures in the standard GUISDAP fits (Blelly et al., 2010; Virtanen et al., 2021).

198

199

200

201

202

203

204

205

The IPY data were collected at the very end of solar cycle 23 close to the sunspot minimum. The median Kp index during the IPY year was 1+, hence the period was mostly geomagnetically quiet. The largest value of the Kp index recorded during the whole year was 6-, which was reached in only two three-hour periods in May 24 and August 6, and there were only 21 3-hour intervals with $Kp \geq 5$. The ESR typically observes the polar cap/cusp ionosphere (Fujiwara et al., 2012), but it may observe also the ionospheric footprint of the closed field lines that connect to the plasma sheet (i.e., the auroral oval), or the different boundary layers in between these regions (Ogawa et al., 2003).

206

3.2 Ion composition fits and the Bayesian Filtering Module

207

208

209

210

211

212

213

214

215

216

217

218

219

220

221

222

In ISR plasma parameter fits, one finds such a combination of plasma parameters that a theoretical autocorrelation function of the incoherent scatter signal, as calculated with the selected parameters, matches with the measurements. In the most general form of the incoherent scatter theory, the theoretical autocorrelation function is a function of the number density, temperature, bulk velocity, and ion-neutral collision frequency of each ion species, the corresponding parameters of the electrons, and the magnetic field (Kudeki & Milla, 2011). Simplifying assumptions are needed in practice, because the measurements do not contain sufficient information for estimating all these parameters. The typical assumptions are that all ion species are in the same temperature and drift with the same velocity, and that the ion composition and collision frequencies are equal to model values calculated e.g. with IRI and MSIS. The magnetic field effects are negligible if the radar beam is not very close to perpendicular to the magnetic field. These assumptions lead to the classical four-parameter fit of N_e, T_e, T_i , and V_i . The four-parameter fit is typically used in "gated" F region incoherent scatter analysis, in which one divides the radar beam into discrete intervals called range gates, and fits plasma parameters to the measured autocorrelation function data separately at each gate.

223

224

225

226

227

228

229

230

The Bayesian Filtering Module (BAFIM) (Virtanen et al., 2021) is an extension module to the standard EISCAT data analysis tool GUISDAP (Lehtinen & Huuskonen, 1996). BAFIM adds properties of full-profile analysis (Holt et al., 1992; Lehtinen et al., 1996), in which one fits plasma parameters along the whole radar beam at once, to the originally gated analysis tool, and extends the idea of full-profile analysis also to time dimension. When analysing EISCAT radar data with combined BAFIM and GUISDAP, one assumes that the plasma parameter profiles are smooth in both altitude and time. These assumptions are justified when the radar beam is field-aligned and the analysis

231 proceeds with reasonably short steps in time. The full-profile analysis alone is known to
 232 enable ion composition fits (Cabrit & Kofman, 1997; Litvine et al., 1998), and the BAFIM
 233 implementation effectively allows one to select resolutions of each plasma parameter sep-
 234 arately (Virtanen et al., 2021). One can thus use coarse resolutions for the ion compo-
 235 sition and thus improve its accuracy, but still solve the other parameters with better res-
 236 olutions.

237 When combined with high range resolution, the original idea of full-profile anal-
 238 ysis leads to a large inverse problem, whose solution is computationally heavy. In the
 239 BAFIM implementation the actual fit is performed at each altitude separately, and the
 240 smoothness assumptions are added by means of Bayesian filtering (Särkkä, 2010, for ex-
 241 ample) and correlation priors (Roininen et al., 2011). This approach keeps the analy-
 242 sis computationally light-weight. The BAFIM analysis proceeds as a sequence of pre-
 243 diction and update steps. In the prediction step, one produces a prior model of the plasma
 244 parameters for the current time step. The prediction is based on the fit results from the
 245 previous time step. In the update step, one runs the normal GUISDAP fit of plasma pa-
 246 rameters using the prediction as a prior. The smoothness assumptions are built in the
 247 prediction step, in which one smooths the plasma parameter profiles in altitude and con-
 248 trols how much the parameters are allowed to change between subsequent time steps.
 249 For details of the BAFIM implementation, see Virtanen et al. (2021).

250 While Virtanen et al. (2021) demonstrated the F₁ region ion composition fits with
 251 BAFIM, it was also noted that the tool is not well suited for rapid ion temperature and
 252 composition variations. This limits also its use in analysis of large data sets, because such
 253 data unavoidably contain also measurements from active conditions. The authors sug-
 254 gested that ion chemistry modeling could be added to the analysis to improve its per-
 255 formance in presence of rapid temperature variations. We note that these issues are re-
 256 lated to the F region ion temperature variations and the TICA in particular, and the tool
 257 has been successfully used for high-resolution E region analysis in presence of rapid elec-
 258 tron density and temperature variations (Tesfaw et al., 2022).

259 3.3 Ion composition fits with BAFIM and IDC

260 The Ion Density Calculator (IDC) (Richards et al., 2010; Richards, 2011) is a chem-
 261 istry model that calculates densities of NO⁺, O₂⁺, N⁺, N₂⁺, and O⁺ ions. The model as-
 262 sumes that all of the ions except O⁺ are in chemical equilibrium, and iteratively finds
 263 such an ion composition that the total number density of all ion species matches with
 264 a known electron density. In our case the electron density is measured with the radar.
 265 The model is based on the chemistry of the Field Line Interhemispheric Plasma (FLIP)
 266 ionosphere model (Richards, 2002) and it is included in the latest versions of the IRI (Bilitza
 267 et al., 2022).

268 The IDC model was originally developed for photoionization, but the model works
 269 also in presence of auroral particle precipitation, because the additional ion production
 270 is implicit in the measured electron density (Richards et al., 2010). Strong ion convec-
 271 tion and the produced increase in ion temperature affect the chemical reaction rates and
 272 may thus become an issue in modeling (Richards et al., 2010). However, as is explained
 273 below, we have coupled the IDC in our analysis tools in such a way that the true tem-
 274 peratures are always used in the model, which guarantees that correct reaction rates are
 275 used also when the ions are heated.

276 We have created an upgraded version of BAFIM that is coupled with the IDC to
 277 improve the ion composition fits. We use this tool to fit five plasma parameters, N_e , T_i ,
 278 $T_r = T_e/T_i$, V_i , and p , to the IPY data. The upgraded BAFIM has two key differences
 279 to the original implementation of Virtanen et al. (2021). First, there is an additional up-
 280 grade step with the IDC after the GUISDAP fit, and second, the plasma parameters con-
 281 sidered as final fit results are those produced by smoothing in altitude.

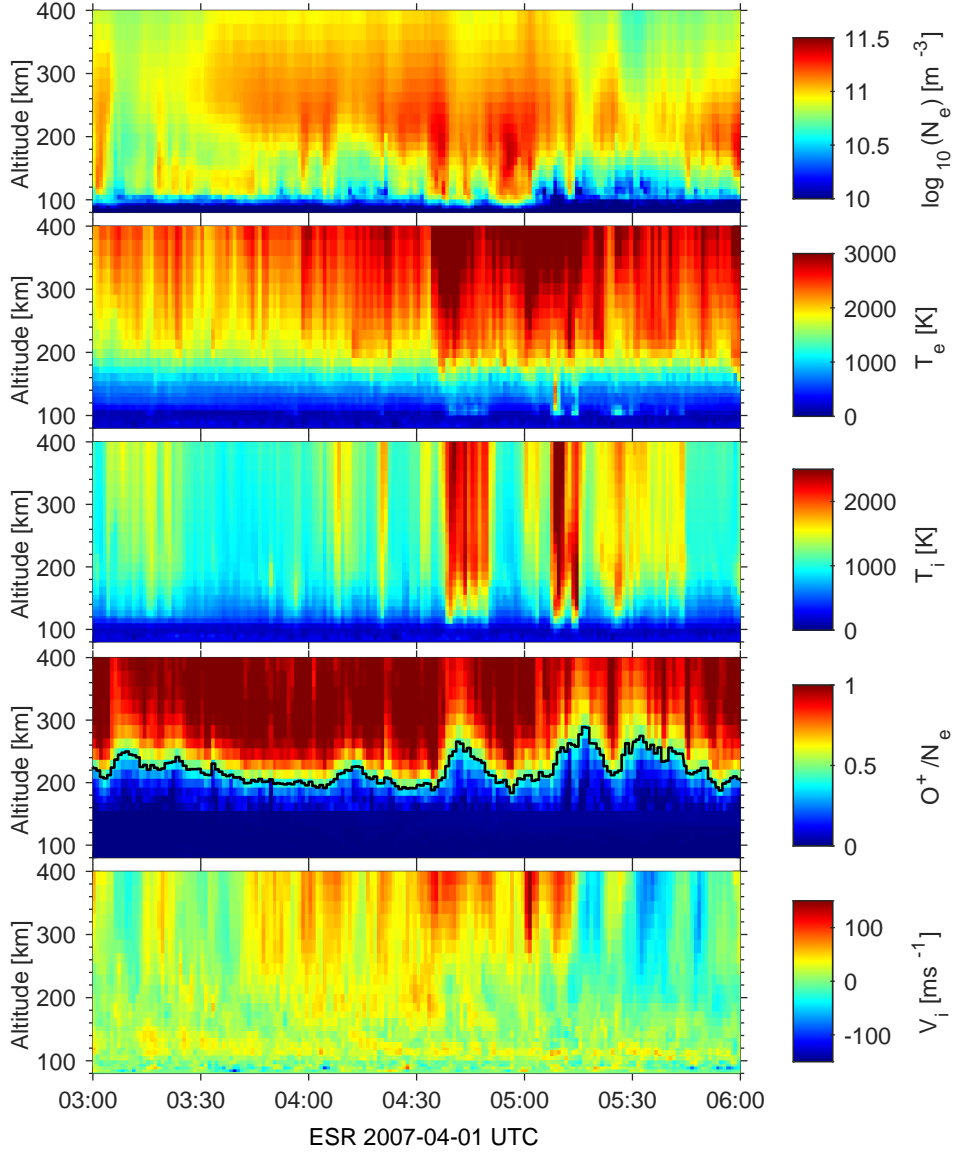


Figure 2. An example of plasma parameter fit results using BAFIM and IDC with GUIDAP from April 2007. From top to bottom, the panels are electron number density, electron temperature, ion temperature, O^+ ion fraction, and line-of-sight plasma velocity (positive away from the radar). The black line in the fourth panel is the molecular-to-atomic transition altitude z_{50} . The solar local time (SLT) is one hour ahead UTC, and the magnetic local time (MLT) is 2.5 hours ahead UTC.

282 In the IDC step we have plasma parameters $\mathbf{x} = (N_e, T_i, T_r, V_i, p)^T$ and their co-
 283 variance matrix \mathbf{P} from the GUIDAP fit. We then look for an updated set of param-
 284 eters $\mathbf{x}' = (N'_e, T'_i, T'_r, V'_i, p')^T$ that minimize the cost function

$$S(\mathbf{x}') = (\mathbf{x} - \mathbf{x}')^T \mathbf{P}^{-1} (\mathbf{x} - \mathbf{x}') + \frac{(p' - p_{IDC}(N'_e, T'_e, T'_i))^2}{\sigma_{IDC}^2}. \quad (5)$$

285 Here p_{IDC} is the fraction of O^+ ions as calculated with the IDC with N'_e , $T'_e = T'_r T'_i$,
 286 and T'_i as inputs. The two terms in (5) are penalties for deviations from the GUIDAP
 287 fit result and the IDC prediction, respectively. The standard deviation σ_{IDC} is selected
 288 by the user and it controls how tightly the updated parameters \mathbf{x}' are bound to the IDC
 289 model predictions. With large σ_{IDC} the model has no effect, and with very small σ_{IDC}
 290 p' is forced to match with the IDC prediction. We have used $\sigma_{IDC} = 0.1$ in this pa-
 291 per. We emphasize that we do not force the compositions to match with the IDC pre-
 292 diction, but due to the first term in (5) the solution is reasonably close to the GUIDAP
 293 fit and the smoothness assumptions of BAFIM are still in place. The final fit results are
 294 plasma parameters \mathbf{x}'' and their covariance matrix \mathbf{P}'' produced by smoothing in alti-
 295 tude by correlation priors, as explained in (Virtanen et al., 2021). The chemistry mod-
 296 eling together with some technical improvements to control of the correlation lengths al-
 297 low us to use considerably longer time steps than those used by Virtanen et al. (2021)
 298 and Tesfaw et al. (2022).

299 The iterative fit with the cost function (5) also guarantees that the ion and elec-
 300 tron temperatures we input to IDC are based on measurements, and that the fitted com-
 301 bination of plasma parameters is reasonable from the chemistry point-of-view. This ap-
 302 proach allows us to avoid the issues with temperature dependent reaction rates mentioned
 303 by Richards et al. (2010). We might still suffer from biases caused by the neutral atmo-
 304 sphere model (NRLMSISE-00), which naturally does not reproduce thermal expansion
 305 of the atmosphere due to short-lived heating events. However, errors in the neutral back-
 306 ground tend to produce non-physical bends in the plasma parameter profiles, and this
 307 effect is thus minimized by the requirement that the profiles must be smooth in altitude.

308 We have analysed the whole IPY data with 60 s time resolution using the combi-
 309 nation of BAFIM and IDC in GUIDAP. Details of the BAFIM settings used in the anal-
 310 ysis and how the input parameters scale with time resolution are give in Appendix A.
 311 An example of the fit results is shown in Figure 2, which contains results from 01 April
 312 2007 03–06 UTC . The figure shows five plasma parameters, N_e , T_e , T_i , p , and V_i as func-
 313 tion of time and altitude. The electron density profiles (top panel) show several clear elec-
 314 tron precipitation events with significant ionization down to the E region. The precip-
 315 itation also heats the electron gas, producing electron temperature enhancements above
 316 150 km altitude (second panel). The ion temperature profiles (third panel) show a group
 317 of strong ion frictional heating events that enhance T_i above 2000 K between 04:30 and
 318 05:30 UTC. Weaker ion heating is seen both before and after the strongest events.

319 The fourth panel of Figure 2 shows the fraction of O^+ ions p and the molecular-
 320 to-atomic transition altitude z_{50} (black line in the fourth panel). The O^+ fraction has
 321 the largest fluctuations at 04:30–06:00 UTC, when both electron precipitation and ion
 322 frictional heating take place. The frictional heating tends to increase z_{50} , which is rapidly
 323 lowered by electron precipitation between the heating events. The bottom panel shows
 324 the line-of-sight plasma velocity, including ion upflows in connection to the energy in-
 325 put by electron precipitation and ion frictional heating. A comparison of our fit result
 326 and the standard GUIDAP fit from the same time interval is provided as supporting
 327 material.

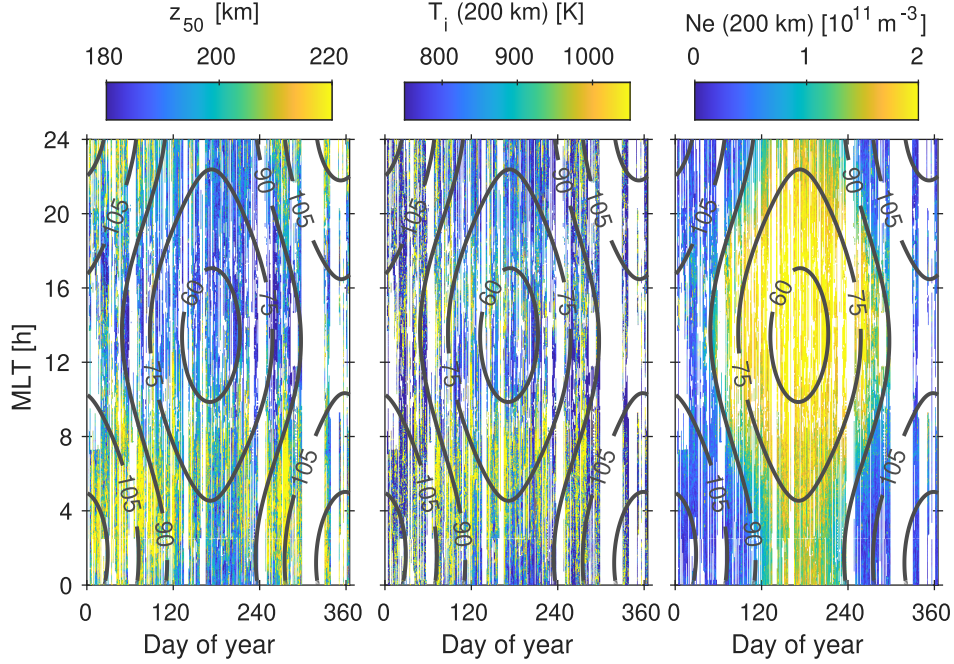


Figure 3. Molecular-to-atomic ion transition altitude (left), ion temperature at 200 km altitude (middle), and electron density at 200 km altitude (right) as function of day of year and magnetic local time. The white areas are missing data due to radar operations in other than the standard IPY mode, or due to technical issues with the radar. Solar zenith angles are shown as contour lines. At 200 km altitude Sun is behind Earth at zenith angles larger than 105° . The solar local time is 1.5 h behind MLT.

4 Statistical results

In this section we present statistical results derived from the IPY data. We concentrate on three key parameters that characterise the F region ion composition variations and their drivers. The parameters are the molecular-to-atomic ion transition altitude z_{50} , ion temperature at 200 km altitude T_i , and electron density at 200 km altitude N_e . The 200 km altitude was selected, because it is close to the average z_{50} . We show also comparisons to model values calculated with the International Reference Ionosphere version 2020, (Bilitza et al., 2022).

4.1 Overview of transition altitudes during the whole year

Figure 3 shows z_{50} , T_i and N_e as function of day of year and magnetic local time (MLT). The MLT has several alternative definitions and it depends on the selected magnetic coordinate system (Laundal & Richmond, 2017). We use the altitude adjusted corrected geomagnetic coordinates (Shepherd, 2014) and calculate the MLT as magnetic longitude difference between the ESR site and a sub-solar point at 700 km altitude. With the ESR coordinates this definition leads to $MLT = UTC + 2.5$ h on average, which we use for the UTC to MLT conversion. As the IPY started in March, days 1–60 are from year 2008, while the rest are from 2007. The figure shows also contours of the solar zenith angle (SZA) overlaid in each panel.

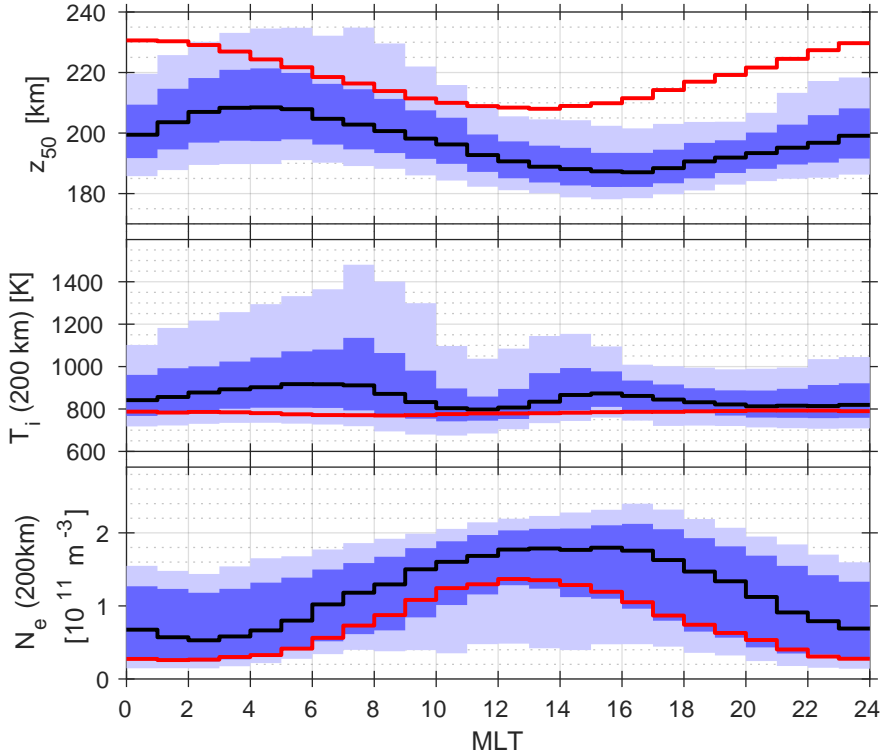


Figure 4. MLT variations of molecular-to-atomic ion transition altitude (top), ion temperature at 200 km altitude (middle) and electron density at 200 km altitude (bottom). The black lines show the median values, the dark blue areas are between 25 % and 75 % percentiles, and the light blue areas are between 10 % and 90 % percentiles. The red lines show medians of IRI-2020 model values.

346 The transition altitudes in the first panel of Figure 3 show a clear diurnal variation,
 347 with largest z_{50} typically observed between magnetic midnight and 10 MLT. The
 348 transition altitudes are generally lower during daytime than at night, and the morning
 349 maxima are lower during summer than during winter. Ion temperature at 200 km alti-
 350 tude (the second panel of Figure 3) shows also a clear diurnal variation with maxima in
 351 the same 00-10 MLT sector with the transition altitude. However, T_i has another local
 352 maximum at 14-17 MLT. Main characteristics of N_e (third panel) follow the solar zenith
 353 angle contours, indicating that the F₁ region electron density is controlled by photoion-
 354 ization. The daytime and summer maxima in N_e match with the minima in z_{50} (first
 355 panel). One should notice that Sun is visible at 200 km altitude when $\text{SZA} < 105^\circ$, which
 356 means that the F region is always sunlit from March to October and for several hours
 357 close to local noon even at mid-winter.

358 4.2 MLT variations in transition altitude

359 The MLT variations of z_{50} , T_i and N_e are shown in more detail in Figure 4, which
 360 shows median values together with 10 %, 25 %, 75 % and 90 % percentiles in 1-hour MLT
 361 bins, as calculated from the whole year of IPY data. The corresponding median values
 362 calculated from IRI model predictions are shown as red lines. The transition altitude in
 363 the first panel of Figure 4 shows a clear diurnal variation with a maximum median value

364 208 km at 04-05 MLT and a minimum value 187 km at 16-17 MLT. The IRI prediction
 365 shows qualitatively similar night maximum and daytime minimum, but their locations
 366 are shifted by about three hours toward earlier MLTs, and the values are up to 32 km
 367 larger than our results. Width of the z_{50} distributions, calculated as difference of the 90 %
 368 and 10 % percentiles, has a maximum of 45 km at 07-08 MLT and a minimum of 20 km
 369 at 19-20 MLT.

370 The MLT variations of T_i are shown in the second panel of Figure 4. While T_i shows
 371 clear diurnal variations, these variations are substantially different from the z_{50} varia-
 372 tions. The ion temperature has two maxima, 920 K at 05-06 MLT and 870 K at 15-16 MLT
 373 in the median values. The 75 % and 90 % percentiles have their maxima closer to noon
 374 than the median values, at 07-08 MLT in the morning side and 14-15 MLT in the af-
 375 ternoon. The ion temperature is very variable in the morning side, and width of the T_i
 376 distribution reaches 760 K at 07-08 MLT. Given that the ion temperature affects the
 377 ion composition via the temperature-dependent reaction rates, one might find the large
 378 difference between the diurnal variations of median T_i and z_{50} surprising. The IRI pre-
 379 diction does not show significant diurnal variations in T_i .

380 An explanation to the different behaviours of z_{50} and T_i is given by the electron
 381 density, shown in the bottom panel of Figure 4. The electron density is strongly controlled
 382 by solar EUV radiation and thus has a dayside maximum after MLT noon and a min-
 383 imum at 02-03 MLT. In the T_i maximum at 15-16 MLT, the high electron density keeps
 384 the fraction of molecular ions and thus also z_{50} low, because the dissociative recomb-
 385 ination of NO^+ and O_2^+ is fast when N_e is large. Although the increased ion tempera-
 386 ture speeds up the rearrangement of atomic O^+ into molecular NO^+ , the molecular ions
 387 are lost so rapidly that their fraction of the total ion content cannot become large. In
 388 the morning hours the electron density is increasing and the z_{50} maximum at 04-05 MLT
 389 is before the T_i maximum at 05-06 MLT, because N_e is lower at 04-05 MLT than an hour
 390 later. The IRI prediction of N_e is generally lower than our measurement and maximizes
 391 earlier, 12-13 MLT. Underestimation of F₁ region N_e by previous versions of IRI in Sval-
 392 bard has been reported by (Bjoland et al., 2016). One can also see that the IRI z_{50} is
 393 controlled by the IRI N_e variations, which may be expected as the IRI T_i is almost con-
 394 stant.

395 4.3 Solar zenith angle dependence of the transition altitude

396 While one may reasonably assume that the MLT variations in ion temperature are
 397 mainly due to the varying location of the radar with respect to the plasma convection
 398 cells, the variations in electron density are largely due to variations in solar illumination.
 399 It is thus illustrative to study the variations also as function of solar zenith angle, as shown
 400 in Figure 5. The data points from before and after local noon are shown separately, be-
 401 cause there is a clear asymmetry between the morning and evening sides.

402 The electron densities in the third panel of figure 5 show a clear SZA dependence
 403 as expected, and the narrow distributions indicate that the density is primarily controlled
 404 by the solar radiation. In the morning side, the densities are almost constant for 125°-
 405 100° zenith angles, and they increase monotonically with decreasing zenith angle for zenith
 406 angles 100°-55°. In the evening side the electron densities are generally larger than in
 407 the morning side, and the densities still decrease also at zenith angles larger than 100°.
 408 This might be due to the long lifetime of the O^+ ions and plasma transport from the day-
 409 side. The zenith angle dependence of N_e continues to angles larger than 90°, because the
 410 solar radiation can still reach the atmosphere due to curvature of the Earth. With 100°
 411 zenith angle the incoming radiation has passed through the ionosphere at 100 km alti-
 tude, which is enough for majority of the ionizing radiation to be absorbed.

413 The ion temperatures in the second panel of figure 5 do not show strong SZA de-
 414 pendence, but they are more variable in the morning side than in the evening side, and

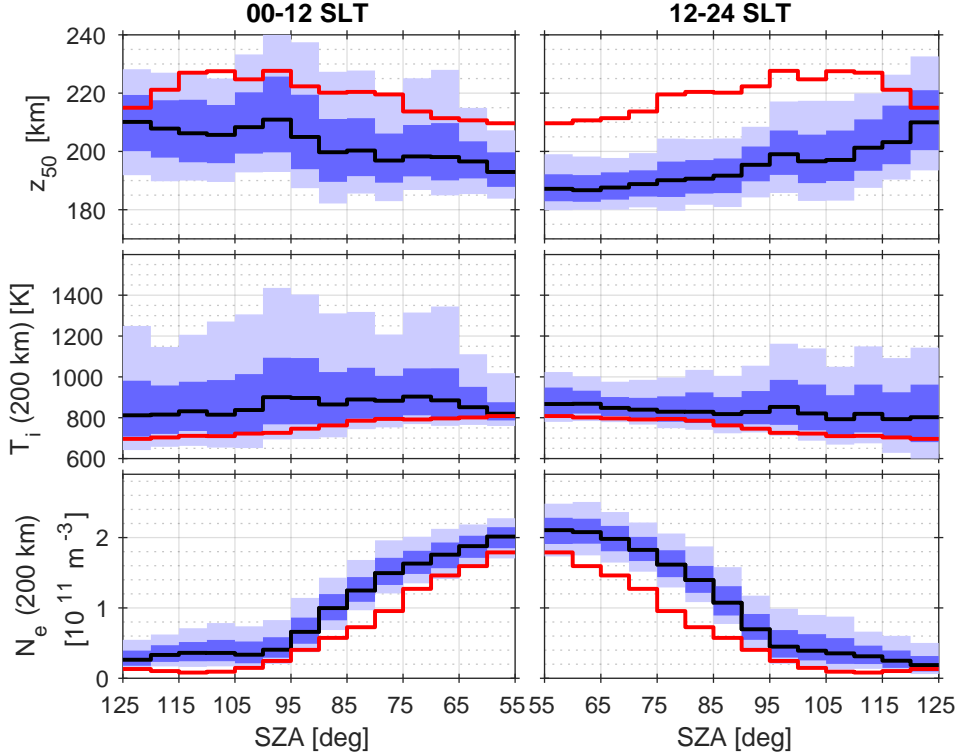


Figure 5. Solar zenith angle variations in the same format as in Figure 4, for morning and evening sides separately.

415 have interesting small maxima at the 90–100° zenith angles. The transition altitude z_{50}
 416 in the first panel of figure 5 shows clear variations with SZA, with smallest and largest
 417 values at smallest and largest zenith angles, correspondingly. The z_{50} variations match
 418 well with those of the electron density, large electron densities corresponding to low z_{50} ,
 419 superimposed with some effects from the relatively stable ion temperature. Like T_i , also
 420 z_{50} shows interesting local maxima close to sunset at 95–100° zenith angles. The mech-
 421 anism that causes the local z_{50} maxima remains unclear, but could be related to atmo-
 422 spheric dynamics or transient ion chemistry effects at the Solar terminator.

423 4.4 Seasonal variations

424 Figure 6 shows median values of z_{50} , T_i and N_e as function of MLT, but separately
 425 for winter, equinoxes, and summer. The seasons are centred on solstices and equinoxes,
 426 and each data point belongs to the season whose centre is closest to it. The spring and
 427 autumn data are merged to form one equinox data set because they behave similarly.
 428 With this division the whole winter has $\text{SZA} \geq 95^\circ$ and the whole summer has $\text{SZA} \leq$
 429 85° , but the equinox data set has twice as much data points as the winter and summer
 430 ones. We note that we have only one year of IPY data and the results thus reflect the
 431 variations typical for a deep solar minimum year.

432 The figure shows that the morning side maxima of z_{50} and T_i are both at 07–08 MLT
 433 on summer. The maxima are at the same time, because the electron density increases
 434 very smoothly with MLT during summer mornings. The overall high N_e in summer also

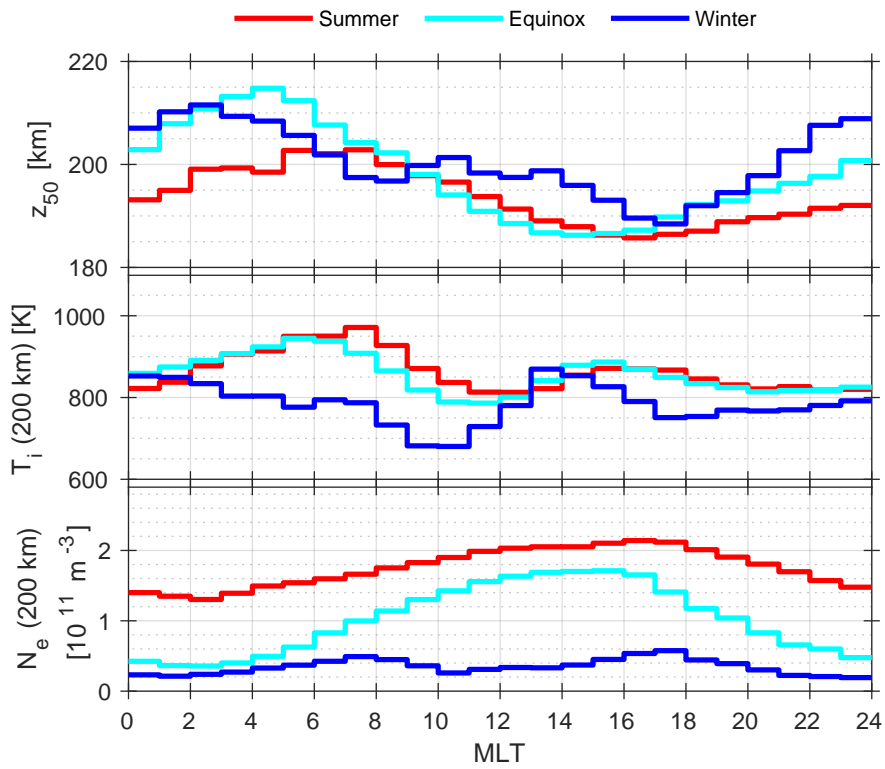


Figure 6. MLT variations of molecular-to-atomic ion transition altitude (top), ion temperature at 200 km altitude (middle), and electron density at 200 km altitude, separately for summer (red), equinoxes (cyan), and winter (blue).

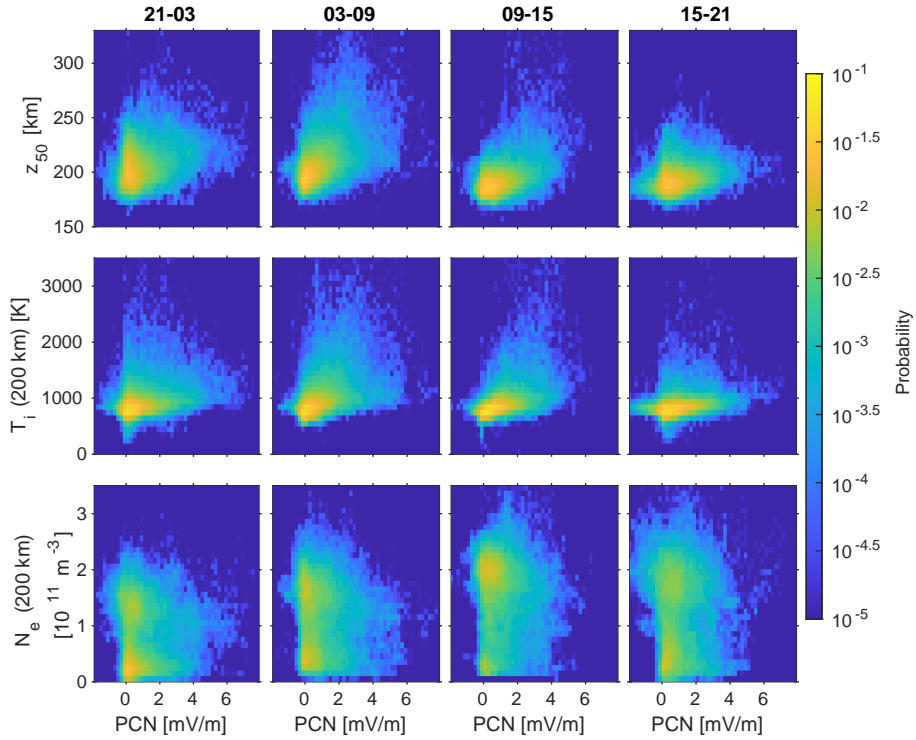


Figure 7. Distribution of fit results as function of the PCN index and the molecular to atomic transition altitudes (top row), the PCN index and ion temperature at 200 km altitude (middle row), and the PCN index and electron density at 200 km altitude (bottom row). Each column of panels corresponds to a SLT bin shown on the top. Notice the logarithmic color scale.

435 favors the atomic ions, and the maximum z_{50} in summer is only 203 km. The evening
 436 side T_i maximum at 16–17 MLT does not create a maximum in transition altitude be-
 437 cause the electron densities are high at this time. During equinoxes, the morning side
 438 T_i maximum moves to 05–06 MLT and the z_{50} maximum of 215 km occurs one hour ear-
 439 lier, 04–05 MLT. The MLT difference is probably due to a large gradient in N_e , which
 440 favours large fractions of molecular ions at earlier MLTs when the electron density is lower.
 441 The evening side maximum in T_i coincides with large N_e also during equinoxes, which
 442 keeps z_{50} low despite the ion heating.

443 The winter data in Figure 6 are quite different from summer and equinoxes. The
 444 transition altitude has a morning side maximum at 02–03 MLT, separated by two hours
 445 from the T_i maximum at 00–01 MLT, but still in a region with relatively high T_i . A dis-
 446 tinct feature of the winter data is a daytime maximum in z_{50} and a corresponding mini-
 447 mum in N_e . The winter time electron densities are very low in general, and the density
 448 has two maxima at 07–08 and 17–18, because photoionization is practically non-existent
 449 and the F region density is created mainly by soft precipitation. The daytime maximum
 450 in z_{50} is caused by the N_e minimum. This phenomenon will be discussed in more detail
 451 in Section 5.1.

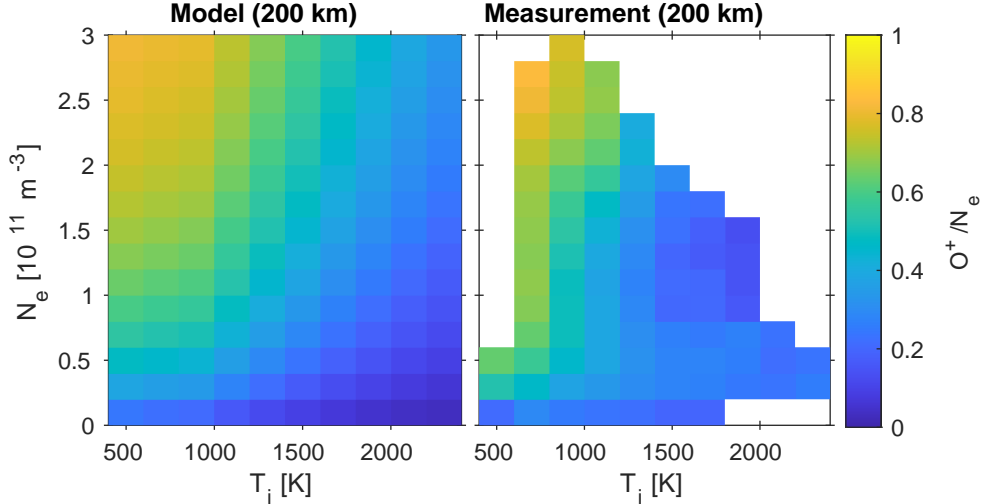


Figure 8. Left: Model results of O^+ ion fraction at 200 km altitude as function of T_i and N_e . The composition is calculated with the IDC model using neutral background atmosphere from NRLMSISE-00 for Svalbard on March 21, 2007 at 05 UTC. Right: Measured O^+ ion fraction at 200 km altitude as function of T_i and N_e . The medians are calculated from one year of ESR data. Only bins that contain at least 100 data points are shown.

452 **4.5 Correlation with geomagnetic activity**

453 As ion temperature is a key parameter that affects the ion composition, one may
 454 reasonably assume that the ion composition should correlate with the level of geomag-
 455 netic activity via increased ion frictional heating. Figure 7 shows distributions of fitted
 456 transition altitudes (top), ion temperatures at 200 km altitude (middle), and electron
 457 densities at 200 km altitude (bottom) as function of the Polar Cap North (PCN) index
 458 (Troshichev et al., 2006). The index is a measure of the solar wind merging electric field
 459 and it estimates the polar cap magnetic activity generated by the solar wind magneto-
 460 sphere interaction. The data are divided into four equally sized blocks according to the
 461 solar local time (SLT = MLT - 1.5 h).

462 The results show that both z_{50} and T_i increase with increasing PCN when PCN
 463 is positive. The strongest response occurs 03–09 SLT and the effect weakens towards the
 464 evening, the weakest response being observed 15–21 SLT. The strongest response to PCN
 465 in both z_{50} and T_i is located in the same local time sector with the generally highest ion
 466 temperatures (Figure 4). This is expected, because the T_i maximum suggests that plasma
 467 convection leads to strongest ion frictional heating in this sector. The response is weaker
 468 in the 09–15 SLT bin, where the electron density is high, and in the 15–21 SLT bin, where
 469 the electron density is higher than in the morning side and the ion temperatures are lower
 470 in general. The electron densities do not show clear PCN dependence.

471 **5 Discussion**

472 **5.1 Effects of N_e and T_i in the F_1 region ion composition**

473 Variations in the molecular-to-atomic ion transition altitude were connected to vari-
 474 ations in electron density and ion temperature in Section 4. It is thus illustrative to study
 475 in more detail how the F_1 region ion composition responds to changes in N_e and T_i . The

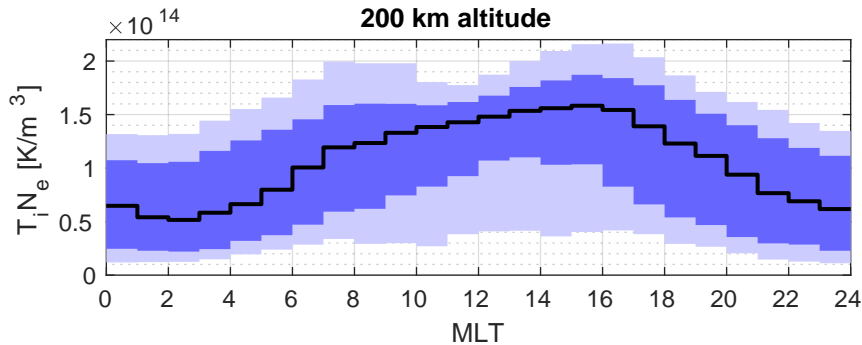


Figure 9. MLT variations of the product $T_i N_e$ (at 200 km). The black line is the median over the whole year, and the shaded areas show the 10 %, 25 %, 75 %, and 90 % percentiles.

476 left panel of Figure 8 shows a model calculation of the fraction of O^+ ions as function
 477 of ion temperature and electron density. Electron and ion temperatures are assumed to
 478 be equal, and the neutral background atmosphere is taken from the NRLMSISE-00 model
 479 for March 21 2007 a 05:00 UTC at 200 km altitude. The results demonstrate how high
 480 electron densities and low ion temperatures favor atomic O^+ ions, while low densities
 481 and high ion temperatures favor the molecular ions, as discussed in the earlier sections.
 482 Regarding the winter daytime maximum in z_{50} , the figure shows that the fraction of O^+
 483 ions is always low when the electron density is of the order of 10^{10}m^{-3} .

484 Distribution of the fitted O^+ fractions at 200 km altitude during the whole IPY
 485 year are shown on the right in Figure 8. The figure is in good qualitative agreement with
 486 the model calculations on the left, which correspond to only one particular instant of time
 487 and neutral background atmosphere. The measurements do not cover all combinations
 488 of T_i and N_e , because solar radiation will necessarily heat the ionosphere so that com-
 489 binations of high N_e and extremely low T_i are impossible, while high T_i speeds up the
 490 recombination and thus prevents the combinations of high T_i and high N_e .

491 5.2 Diurnal variations of transition altitude and ion temperature

492 The Joule heating pattern in the auroral oval is known to have maxima in the dawn
 493 side and in the dusk side, due to convection electric fields (Cai et al., 2016, and refer-
 494 ences therein). However, the ESR is typically in the polar cap, and Cai et al. (2016) found
 495 only the afternoon Joule heating maximum around 15 MLT from ESR measurements.
 496 The Joule heating pattern observed by Cai et al. (2016) thus cannot directly explain our
 497 observations of z_{50} , which peaks in the morning side, and T_i , which has two maxima.

498 A key difference between our results and the Joule heating studies is that the ion
 499 temperature is proportional to kinetic energy per particle, while the Joule heating rates
 500 are expressed as power per unit volume. The same Joule heating rate may thus lead to
 501 different ion temperatures, depending on the ion (electron) density. In our data the morn-
 502 ing side ion temperature maximum at 05–07 MLT (Figure 4) is actually larger than the
 503 afternoon maximum at 15–16 MLT, but N_e is considerably lower around the morning
 504 side maximum. The morning side T_i maximum may thus be generated with consider-
 505 ably smaller heating power per unit volume than the afternoon maximum. This is demon-
 506 strated in Figure 9, which shows the product $T_i N_e$ as function of MLT. The product is
 507 proportional to the kinetic energy per unit volume and can thus be compared with Joule
 508 heating rates. The median values of $T_i N_e$ do not have a morning side maximum, because
 509 the T_i maximum is smoothed out by the lower N_e . The product has maximum at 15–

510 16 MLT, which is exactly the MLT bin where Cai et al. (2016) found the afternoon hot
511 spot in Joule heating.

512 The afternoon hot spot in Joule heating does not create a z_{50} maximum in sum-
513 mer and equinoxes (see Figure 6), because ion production by photoionization keeps the
514 electron density high, which favours the atomic ions. An exception is winter, when there
515 is no photoionization and z_{50} is clearly elevated close to the afternoon maximum in T_i ,
516 as one can see from Figure 6. However, the day-side maximum in z_{50} does not coincide
517 with the afternoon maximum in T_i even at winter, because the very low electron den-
518 sity between 10 and 11 MLT creates the z_{50} maximum there.

519 The morning side maximum in Joule heating creates both T_i and z_{50} maxima in
520 all seasons, as illustrated in Figure 6. This is because the electron densities are gener-
521 ally lower before 8 MLT than 13–16 MLT. The effect of electron density is still visible
522 also in the morning side maximum, where the transition altitudes are clearly lower in
523 summer than during other seasons, because the electron densities in the 00–08 MLT sec-
524 tor are much higher in summer than at other times of the year.

525 **5.3 Limitations of the analysis method and potential future work**

526 The BAFIM analysis assumes that the plasma parameters vary smoothly in both
527 time and range (altitude). Incorrect use of such assumptions could obviously lead to in-
528 correct analysis results if sharp gradients were present in the ionosphere. In BAFIM the
529 smoothness is expressed in terms of probabilities, and also relatively sharp gradients may
530 be produced if the measurements give strong enough evidence about their existence. For
531 example, relatively sharp temporal gradients are seen in all plasma parameters in Fig-
532 ure 2. The assumption of smoothness in range is well justified in field-aligned observa-
533 tions, because the high ion and electron mobilities along the field-line prevent genera-
534 tion of large gradients. The gradients tend to be larger in the E and lower F regions than
535 above, which we take into account by means of using shorter correlation lengths in these
536 regions (Virtanen et al., 2021). We thus believe that the smoothness assumptions do not
537 significantly bias the results from field-aligned observations, but the method may not be
538 applicable to other beam directions in its present form. However, prior models very sim-
539 ilar to those used in BAFIM are used for 4-dimensional (three spatial dimensions plus
540 time) ionospheric tomography (Norberg et al., 2023). These techniques could possibly
541 be generalized to volumetric plasma parameter fits with the multi-beam EISCAT3D radar
542 (McCrea et al., 2015).

543 The IDC assumes chemical equilibrium of all other ion species except O^+ , and takes
544 the neutral background atmosphere from the empirical NRLMSISE-00 model. These as-
545 sumptions may affect the chemistry modeling in active conditions, in which the chem-
546 istry may not have time to reach equilibrium, and energy input from the magnetosphere
547 may lead to thermal expansion of the neutral atmosphere. The way we have coupled BAFIM
548 and IDC reduces these effects to the smallest possible level, because IDC is used merely
549 to guide the solver toward a physically reasonable solution, and the smoothness assump-
550 tions in BAFIM efficiently suppress artifacts created by inaccurate chemistry modeling.
551 For example, the chemistry modeling could overestimate the fraction of molecular ions
552 in very short-lived frictional heating events, during which the ionosphere is not in chem-
553 ical equilibrium. However, the overestimation would lead to unrealistic local ion tem-
554 perature maxima, which would be suppressed by the smoothness assumptions.

555 We implicitly assume that the true average ion temperature can be estimated from
556 the field-aligned radar data using a standard incoherent scatter theory that assumes Maxwellian
557 particle velocity distributions. This assumption may not be valid during very strong heat-
558 ing events, which generate T_i anisotropies with higher T_i in the directions perpendicu-
559 lar to the magnetic field than along the field, and toroidal ion velocity distributions in
560 the F region (Goodwin et al., 2014, and references therein). The average ion tempera-

561 ture that is relevant for the chemistry might thus be larger than the field-aligned tem-
 562 perature extracted from the radar data, and even the field-aligned temperature could
 563 be biased in the worst case. Ion temperature anisotropies could thus lead to underes-
 564 timation of molecular ion content during intense heating events. As the T_i anisotropy
 565 takes place throughout the F region, it might not create noticeable artifacts in the plasma
 566 parameter profiles. While the T_i anisotropies might have a significant effect during some
 567 very strong heating events, vast majority of our data are measured in relatively quiet ge-
 568 omagnetic conditions and are free from the temperature anisotropy effects. However, this
 569 effect is worth considering if one studies strong, individual heating events.

570 6 Conclusions

571 In this paper, we have developed a new analysis tool for IS radar data by coupling
 572 the BAFIM tool (Virtanen et al., 2021) with the IDC ion chemistry model (Richards et
 573 al., 2010; Richards, 2011). By using the tool, we have fitted the F₁ region O⁺ ion frac-
 574 tions (O^+/N_e) to one year of EISCAT Svalbard radar IPY data from March 2007 to Febru-
 575 ary 2008 close to solar minimum.

576 When averaged over the whole year, the molecular-to-atomic ion transition alti-
 577 tude z_{50} undergoes diurnal variations with a maximum median value of 208 km at 04–
 578 05 MLT and a minimum of 187 km at 16–17 MLT. The diurnal variation in z_{50} is a com-
 579 bined effect of variations in T_i and N_e . Increasing T_i tends to increase z_{50} , while increas-
 580 ing N_e tends to decrease it. T_i has two maxima, 920 K at 05–06 MLT and 870 K at 15–
 581 16 MLT, but the global maximum in z_{50} is already 04–05 MLT when N_e is smaller than
 582 closer to the noon. The T_i maximum at 15–16 MLT does not increase z_{50} , because the
 583 high N_e during these MLTs favors the atomic O⁺ ions.

584 We find that the electron density follows variations in the solar zenith angle, in-
 585 dicated that photoionization is the dominant electron production mechanism. An ex-
 586 ception is the winter, when photoionization is very weak and N_e has a daytime minimum
 587 surrounded by weak maxima at 07–08 MLT and 17–18 MLT. These maxima are prob-
 588 ably caused by soft precipitation. The very low daytime N_e leads to anomalously large
 589 fraction of molecular ions in the winter daytime F₁ region.

590 The ion temperature and the molecular-to-atomic transition altitude show corre-
 591 lation with the Polar Cap North (PCN) geomagnetic index. The strongest correlations
 592 are observed 03–09 SLT, which is close to the morning side maximum in T_i . The weak-
 593 est response is seen 15–21 SLT, when N_e is high and T_i relatively low, in average. The
 594 electron density does not show significant response to PCN.

595 Our observed z_{50} is clearly different from that predicted by the International Ref-
 596 erence Ionosphere. The IRI predictions show MLT variations qualitatively similar with
 597 our results, but the annual median values are 14–32 km larger in IRI than in our obser-
 598 vations, and the maximum and minimum values are at 3 hours earlier MLTs. These dif-
 599 ferences are related to the generally lower T_i and N_e in IRI than in our measurements,
 600 and to lack of diurnal T_i variations in IRI.

601 7 Open Research

602 A download link to BAFIM will be provided upon acceptance of the manuscript.
 603 We use the Flipchem python interface to the IDC package (Reimer et al., 2021), avail-
 604 able from <https://doi.org/10.5281/zenodo.3688853>. The EISCAT data are avail-
 605 able for download from the EISCAT data server: <https://portal.eiscat.se/schedule/>.

Table A1. BAFIM settings used in the data analysis. N_e, T_i, T_r , and V_i are fitted at all altitudes above h_{min} . The constants s^h and s^t are scaling factors that control smoothness of the solutions in range and time, respectively, as explained in the text.

	s^h ($s^{-1/2}$)	s^t	h_{min} (km)	h_{max} (km)
N_e	0.05	$2.5 \cdot 10^{11} \text{ m}^{-3} \text{ s}^{-1/2}$	0	-
T_i	0.1	$30 \text{ K s}^{-1/2}$	80	-
T_r	0.1	$0.03 \text{ s}^{-1/2}$	97	-
V_i	0.05	$2.5 \text{ ms}^{-3/2}$	80	-
p	0.05	$0.01 \text{ s}^{-1/2}$	150	500

Appendix A BAFIM settings

For this work the BAFIM implementation of Virtanen et al. (2021) was slightly modified to make the tool better suited for the large-scale data analysis and to couple it with the IDC model. For description of the coupling with the IDC we refer to Section 3.3, and for the general BAFIM implementation we refer to Virtanen et al. (2021). In this section we describe the length scales and time scales used to control smoothness in altitude and time, and how these were changed from Virtanen et al. (2021).

As explained in Section 3 of Virtanen et al. (2021), the smoothness in altitude is controlled by means of the lengths scales s_i^h , where the index i refers to each fitted plasma parameter, and the smoothness in time is controlled by a similar scaling factors s_i^t . The final correlation lengths in altitude are products $s_i^h H$, where H is the local plasma scale height, and the final process noise variance in the Bayesian filtering is the product $(s_i^t)^2 \Delta t$, where Δt is the time step duration. The correlation priors (Roininen et al., 2011) make the smoothing in altitude independent from the altitude resolution, and the process noise variances scale with the time step duration to adjust for different time resolutions.

One remaining effect that was not considered by Virtanen et al. (2021) is that the correlations in time introduced by the Bayesian filtering propagate information about smoothness in altitude in between adjacent time steps. The smoothing in altitude was thus stronger than one could expect based on the correlation lengths alone. The effect becomes clearly visible when one moves from the approximately 5 s time resolution of (Virtanen et al., 2021) to the 60 s resolution used in this paper. To accommodate for this effect, we multiply the length scales s_i^h by square root of the time step duration Δt . The length scales are thus given in units $s^{-1/2}$ and the final correlation length is the product $s_i^h \Delta t^{-1/2} H$. The parameters used in the BAFIM analysis presented in this paper are listed in Table A1.

Acknowledgments

We acknowledge the EISCAT Scientific Association for the radar data. EISCAT is an international association supported by research organisations in China (CRIRP), Finland (SA), Japan (NIPR and ISEE), Norway (NFR), Sweden (VR), and the United Kingdom (UKRI). The authors wish to acknowledge CSC – IT Center for Science, Finland, for computational resources. This work was supported by the Kvantum Institute of the University of Oulu, by the Academy of Finland (347796 and 24304299), and by the Vilho, Yrjö and Kalle Väisälä foundation of the Finnish Academy of Science and Letters.

References

Aponte, N., Sulzer, M. P., Nicolls, M. J., Nikoukar, R., & González, S. A. (2007).

- 641 Molecular ion composition measurements in the F1 region at Arecibo. *Journal of Geophysical Research: Space Physics*, 112(6), 1–18. doi: 10.1029/2006JA012028
- 642
- 643
- 644 Bilitza, D., Pezzopane, M., Truhlik, V., Altadill, D., Reinisch, B. W., & Pignalleri, A. (2022). The International Reference Ionosphere model: A review and description of an ionospheric benchmark. *Reviews of Geophysics*. doi: 10.1029/2022RG000792
- 645
- 646
- 647
- 648 Bjoland, L. M., Belyey, V., Løvhaug, U. P., & La Hoz, C. (2016, 9). An evaluation of International Reference Ionosphere electron density in the polar cap and cusp using EISCAT Svalbard radar measurements. *Annales Geophysicae*, 34(9), 751–758. doi: 10.5194/angeo-34-751-2016
- 649
- 650
- 651
- 652 Bjørnå, N., & Kirkwood, S. (1988). Derivation of ion composition from a combined ion line/plasma line incoherent scatter experiment. *Journal of Geophysical Research*, 93(A6), 5787. doi: 10.1029/JA093iA06p05787
- 653
- 654
- 655 Brelvy, P. L., Alcaydé, D., & Van Eyken, A. P. (2010). A new analysis method for determining polar ionosphere and upper atmosphere characteristics from ESR data: Illustration with IPY period. *Journal of Geophysical Research: Space Physics*, 115(9), 1–12. doi: 10.1029/2009JA014876
- 656
- 657
- 658
- 659 Cabrit, B., & Kofman, W. (1997). Ionospheric composition measurement by EISCAT using a global fit procedure. *Annales Geophysicae*, 14(12), 1496–1505. doi: 10.1007/s00585-996-1496-2
- 660
- 661
- 662 Cai, L., Aikio, A. T., & Milan, S. E. (2016). Joule heating hot spot at high latitudes in the afternoon sector. *Journal of Geophysical Research: Space Physics*, 121(7), 7135–7152. doi: 10.1002/2016JA022432
- 663
- 664
- 665 Evans, J. V. (1967, 7). Electron temperature and ion composition in the F1 region. *Journal of Geophysical Research*, 72(13), 3343–3355. doi: 10.1029/jz072i013p03343
- 666
- 667
- 668 Fredriksen, (1990). High latitude quiet summer ion composition profiles derived from a combined ion line/plasma line incoherent scatter experiment. *Journal of Atmospheric and Terrestrial Physics*, 52(1), 77–84. doi: 10.1016/0021-9169(90)90117-6
- 669
- 670
- 671
- 672 Fujiwara, H., Nozawa, S., Maeda, S., Ogawa, Y., Miyoshi, Y., Jin, H., ... Terada, K. (2012). Polar cap ionosphere and thermosphere during the solar minimum period: EISCAT Svalbard radar observations and GCM simulations. *Earth, Planets and Space*, 64(6), 459–465. doi: 10.5047/eps.2011.05.023
- 673
- 674
- 675
- 676 Goodwin, L., St.-Maurice, J. P., Richards, P., Nicolls, M., & Hairston, M. (2014). F region dusk ion temperature spikes at the equatorward edge of the high-latitude convection pattern. *Geophysical Research Letters*, 41(2), 300–307. doi: 10.1002/2013GL058442
- 677
- 678
- 679
- 680 Häggström, I., & Collis, P. (1990). Ion composition changes during F-region density depletions in the presence of electric fields at auroral latitudes. *Journal of Atmospheric and Terrestrial Physics*, 52(6-8), 519–529. doi: 10.1016/0021-9169(90)90050-W
- 681
- 682
- 683
- 684 Holt, J. M., Rhoda, D. A., Tetenbaum, D., & van Eyken, A. P. (1992). Optimal analysis of incoherent scatter radar data. *Radio Science*, 27(3), 435–447. doi: 10.1029/91RS02922
- 685
- 686
- 687 Huuskonen, A., Lehtinen, M. S., & Pirttilä, J. (1996). Fractional lags in alternating codes: Improving incoherent scatter measurements by using lag estimates at noninteger multiples of baud length. *Radio Science*, 31(2), 245–261. doi: 10.1029/95RS03157
- 688
- 689
- 690
- 691 Kelly, J. D., & Wickwar, V. B. (1981). Radar measurements of high-latitude ion composition between 140 and 300 km altitude. *Journal of Geophysical Research: Space Physics*, 86(A9), 7617–7626. doi: 10.1029/JA086iA09p07617
- 692
- 693
- 694 Kudeki, E., & Milla, M. A. (2011). Incoherent scatter spectral theories - Part I: A general framework and results for small magnetic aspect angles. *IEEE Trans-*
- 695

- 696 *actions on Geoscience and Remote Sensing*, 49(1 PART 2), 315–328. doi: 10
697 .1109/TGRS.2010.2057252
- 698 Lathuillere, C., Lejeune, G., & Kofman, W. (1983). Direct measurements of ion
699 composition with EISCAT in the high-latitude F1 region. *Radio Science*,
700 18(6), 887–893. doi: 10.1029/RS018i006p00887
- 701 Lathuillere, C., & Pibaret, B. (1992). *A statistical model of ion composition in the*
702 *auroral lower F region* (Vol. 12; Tech. Rep. No. 6). doi: 10.1016/0273-1177(92)
703 90048-3
- 704 Laundal, K. M., & Richmond, A. D. (2017, 3). Magnetic Coordinate Systems. *Space*
705 *Science Reviews*, 206(1-4), 27–59. doi: 10.1007/s11214-016-0275-y
- 706 Lehtinen, M. S., & Häggström, I. (1987). A new modulation principle for inco-
707 herent scatter measurements. *Radio Science*, 22(4), 625–634. doi: 10.1029/
708 RS022i004p00625
- 709 Lehtinen, M. S., & Huuskonen, A. (1996). General incoherent scatter analysis and
710 GUISDAP. *Journal of Atmospheric and Terrestrial Physics*, 58(1-4), 435–452.
711 doi: 10.1016/0021-9169(95)00047-X
- 712 Lehtinen, M. S., Huuskonen, A., & Pirttilä, J. (1996). First experiences of full-profile
713 analysis with GUISDAP. *Annales Geophysicae*, 14(12), 1487–1495. doi: 10
714 .1007/s00585-996-1487-3
- 715 Litvine, A., Kofman, W., & Cabrit, B. (1998). Ion composition measurements and
716 modelling at altitudes from 140 to 350 km using EISCAT measurements. *An-*
717 *nales Geophysicae*, 16(10), 1159. doi: 10.1007/s005850050685
- 718 Martínez-Ledesma, M., & Díaz Quezada, M. A. (2019). Determination of the Signal
719 Fluctuation Threshold of the Temperature-Ion Composition Ambiguity Prob-
720 lem Using Monte Carlo Simulations. *Journal of Geophysical Research: Space*
721 *Physics*, 124(4), 2897–2919. doi: 10.1029/2018JA026217
- 722 McCrea, I., Aikio, A., Alfonsi, L., Belova, E., Buchert, S., Clilverd, M., ... Vierinen,
723 J. (2015, 12). The science case for the EISCAT 3D radar. *Progress in Earth*
724 *and Planetary Science*, 2(1), 21. doi: 10.1186/s40645-015-0051-8
- 725 Norberg, J., Käki, S., Roininen, L., Mielich, J., & Virtanen, I. I. (2023, 1). Model-
726 Free Approach for Regional Ionospheric Multi-Instrument Imaging. *Journal of*
727 *Geophysical Research: Space Physics*, 128(1). doi: 10.1029/2022JA030794
- 728 Ogawa, Y., Fujii, R., Buchert, S. C., Nozawa, S., & Ohtani, S. (2003). Simultaneous
729 EISCAT Svalbard radar and DMSP observations of ion upflow in the dayside
730 polar ionosphere. *Journal of Geophysical Research: Space Physics*, 108(A3).
731 doi: 10.1029/2002JA009590
- 732 Picone, J. M., Hedin, A. E., Drob, D. P., & Aikin, A. C. (2002). NRLMSISE-00
733 empirical model of the atmosphere: Statistical comparisons and scientific is-
734 sues. *Journal of Geophysical Research: Space Physics*, 107(A12), 1–16. doi:
735 10.1029/2002JA009430
- 736 Reimer, A., amisr user, & FGuenzkofer. (2021, November). *amisr/flipchem:*
737 *v2021.2.2 bugfix release*. Zenodo. doi: 10.5281/zenodo.5719844
- 738 Richards, P. G. (2002). Ion and neutral density variations during ionospheric storms
739 in September 1974: Comparison of measurement and models. *Journal of Geo-*
740 *physical Research: Space Physics*, 107(A11). doi: 10.1029/2002JA009278
- 741 Richards, P. G. (2011). Reexamination of ionospheric photochemistry. *Jour-*
742 *nal of Geophysical Research: Space Physics*, 116(8), 1–15. doi: 10.1029/
743 2011JA016613
- 744 Richards, P. G., Bilitza, D., & Voglozin, D. (2010). Ion density calculator (IDC):
745 A new efficient model of ionospheric ion densities. *Radio Science*, 45(5), 1–11.
746 doi: 10.1029/2009RS004332
- 747 Richards, P. G., Nicolls, M. J., Heinselman, C. J., Sojka, J. J., Holt, J. M., & Meier,
748 R. R. (2009). Measured and modeled ionospheric densities, temperatures, and
749 winds during the international polar year. *Journal of Geophysical Research:*
750 *Space Physics*, 114(12). doi: 10.1029/2009JA014625

- 751 Roininen, L., Lehtinen, M. S., Lasanen, S., Orispää, M., & Markkanen, M. (2011).
752 Correlation priors. *Inverse Problems and Imaging*, 5(1), 167–184. doi: 10
753 .3934/ipi.2011.5.167
- 754 Särkkä, S. (2010). Bayesian filtering and smoothing. *Bayesian Filtering and Smooth-*
755 *ing*, 1–232. doi: 10.1017/CBO9781139344203
- 756 Shepherd, S. G. (2014, 9). Altitude-adjusted corrected geomagnetic coordinates:
757 Definition and functional approximations. *Journal of Geophysical Research:*
758 *Space Physics*, 119(9), 7501–7521. doi: 10.1002/2014JA020264
- 759 Shibata, T., Matsuya, H., & Hoashi, J. (2000). *Ion composition in the auroral*
760 *lower F-region inferred from residuals of ion temperature profiles observed with*
761 *EISCAT* (Vol. 25; Tech. Rep. No. I). doi: 10.1016/S0273-1177(99)00919-9
- 762 Takada, M., Seki, K., Ogawa, Y., Keika, K., Kasahara, S., Yokota, S., . . . Shino-
763 hara, I. (2021). Low-Altitude Ion Upflow Observed by EISCAT and its
764 Effects on Supply of Molecular Ions in the Ring Current Detected by Arase
765 (ERG). *Journal of Geophysical Research: Space Physics*, 126(5), 1–12. doi:
766 10.1029/2020JA028951
- 767 Tesfaw, H. W., Virtanen, I. I., Aikio, A. T., Nel, A., Kosch, M., & Ogawa, Y.
768 (2022). Precipitating Electron Energy Spectra and Auroral Power Estimation
769 by Incoherent Scatter Radar With High Temporal Resolution. *Journal of Geo-*
770 *physical Research: Space Physics*, 127(4), 1–18. doi: 10.1029/2021ja029880
- 771 Troshichev, O., Janzhura, A., & Stauning, P. (2006, 5). Unified PCN and PCS
772 indices: Method of calculation, physical sense, and dependence on the IMF
773 azimuthal and northward components. *Journal of Geophysical Research: Space*
774 *Physics*, 111(5). doi: 10.1029/2005JA011402
- 775 Virtanen, I. I., Tesfaw, H. W., Roininen, L., Lasanen, S., & Aikio, A. (2021).
776 Bayesian Filtering in Incoherent Scatter Plasma Parameter Fits. *Jour-*
777 *nal of Geophysical Research: Space Physics*, 126(3), 1–13. doi: 10.1029/
778 2020JA028700
- 779 Zettergren, M., Semeter, J., Burnett, B., Oliver, W., Heinselman, C., Blelly, P. L.,
780 & Diaz, M. (2010). Dynamic variability in F-region ionospheric composi-
781 tion at auroral arc boundaries. *Annales Geophysicae*, 28(2), 651–664. doi:
782 10.5194/angeo-28-651-2010